JOURNAL OF COMPUTATIONAL PHYSICS 122, 107–117 (1995)

Multigrid Calculation of Steady, Viscous Flow in a Triangular Cavity

R. JYOTSNA AND S. P. VANKA

Department of Mechanical and Industrial Engineering, University of Illinois at Urbana-Champaign, Urbana, Illinois 61801

Received January 3, 1995; revised April 25, 1995

Lid-driven recirculating flow in a triangular cavity is simulated at different Reynolds numbers, using a multigrid solution procedure for the Navier–Stokes equations discretized on triangular grids. The discretization uses a control volume methodology, with linear internodal variation of the flow variables. The use of the multigrid technique provides rapid and grid-independent rates of convergence. Richardson extrapolation is used to obtain accurate representations of the flow field for all reported Reynolds numbers. The most significant feature of the flow is the occurrence of a sequence of eddies of rapidly decreasing intensity towards the stationary lower corner of the cavity. Streamtraces of the eddies, contours of vorticity, and plots of the centerline velocity and pressure are presented. The solution at low Reynolds numbers is compared with the analytical results of Moffat. © 1995 Academic Press, Inc.

1. INTRODUCTION

Shear driven flow in a square cavity has been the object of a large number of numerical studies in computational fluid dynamics (cf. [1–7]). Here, the recirculating flow of the enclosed viscous fluid is driven by the shearing motion of the top wall, which is translated at a uniform velocity. The attention this problem has received is largely due to the simplicity of the geometry and boundary conditions, coupled with the interesting flow features observed at different Reynolds numbers. It has been repeatedly used to test new developments in numerical methods for internal flows. Perhaps the most comprehensive study of the flow field and eddies at different Reynolds numbers is that due to Ghia *et al.* [5].

There have been fewer numerical studies of the driven cavity problem in complex geometries, although such geometries are encountered in a variety of engineering equipment such as automotive passages, heating ducts with fins, inlets, and combustors. In particular, sharp corners are associated with many of these geometries. An idealization of flow near a sharp corner is the driven cavity problem in a triangular geometry, which has been investigated here.

The apparent lack of interest in geometries other than the square, is mainly due to difficulties encountered in representing the complex flow geometries using structured grids. There have, however, been a few studies of flow in curved and nonrectangular geometries. Recently, Vynnycky and Kimura [8] reported the results of their study of steady flow in a driven quarter-circular cavity. In an earlier work, Ribbens *et al.* [9] described the flow in an elliptic region with a moving boundary. The flow in a trapezoidal cavity was studied by Darr and Vanka [10]. Although curved and nonrectangular geometries may be represented using curvilinear and nonorthogonal structured grids, the triangular cavity is an example that poses a severe test for structured grid-based numerical methods. Many of the problems encountered have been explained in detail by Ribbens *et al.* [11]. Their problems arose mainly from the treatment of the corners, which gave rise to singular systems of equations for the centered finite difference and colocation schemes that they attempted. Even the scheme which was finally used successfully for the equilateral triangle, by transforming the problem to an equivalent one on an isosceles right triangle, was expected to lead to a singular problem for a scalene triangle. No such problems are encountered with the use of triangular grids as presented here. The corners do not require special treatment, and the numerical scheme reduces to a straightforward procedure for any geometry.

The triangular cavity also exhibits interesting flow features that have been analytically studied by Moffat [12] in the Stokes regime and by Batchelor [13] in the inviscid or infinite Reynolds number regime. The most interesting feature of the flow is the occurrence of an infinite sequence of eddies of decreasing size and rapidly decreasing intensity towards the stationary corner. Because of the rapid decrease in eddy size and intensity towards the corner, it is difficult to resolve more than a few eddies either experimentally or numerically. However, they can be determined analytically for Stokes flow, which is a reasonable representation of the flow field near the stationary corner [12]. Moffat [12] has also shown that sufficiently close to the corner, the flow is independent of that in the farther regions, and the intensities of the eddies as well as their distances from the corner follow geometric sequences. This was indeed observed in the present computation and will be discussed in the results section. At infinite Reynolds number, Batchelor [13] has shown that the interior region attains constant vorticity.

In the following sections, we will first present the details of the numerical procedure employed to solve the governing

0021-9991/95 $12.00
Copyright © 1995 by Academic Press, Inc.
All rights of reproduction in any form reserved.

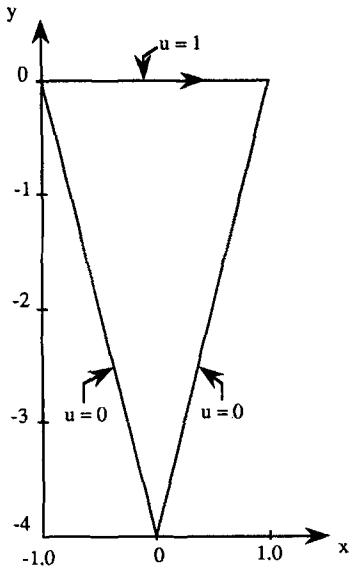

FIG. 1. Geometry and coordinate system for the triangular cavity.

equations, with a brief description of the multigrid strategy used for accelerating the rate of convergence. In the next section, the results of the computations at different Reynolds numbers will be presented, in the form of plots of the streamtraces in the flow field, constant vorticity contours, the centerline velocities and pressures, and the location of the eddies. Grid independent results will be presented by Richardson extrapolation, using the results obtained on two consecutive grids.

2. GOVERNING EQUATIONS AND NUMERICAL PROCEDURE

Figure 1 shows the geometry of the triangular cavity, with the coordinate system used here. Although Ribbens *et al.* [11] performed their study in an equilateral triangle, here we have used a smaller angle at the stationary corner, in order to capture more of the eddies and to verify Moffat's [12] predictions. In the flow region, we solve the Navier–Stokes equations governing a two-dimensional, steady, incompressible flow of constant fluid properties. These equations are written in primitive variables (u, v, p) as

$$\nabla \cdot (\mathbf{u}u) = -(\partial p/\partial x) + \nu \nabla \cdot (\nabla u) + B_u \tag{1}$$

$$\nabla \cdot (\mathbf{u}v) = -(\partial p/\partial y) + \nu \nabla \cdot (\nabla v) + B_v \tag{2}$$

$$\nabla \cdot \mathbf{u} = 0 \tag{3}$$

Here u and v are the two components of the velocity vector $\mathbf{u}$, and p is the pressure divided by the density; ν is the kinematic viscosity, and B_u and B_v provide a means to include other forces such as those due to gravity and rotation.

The above equations are discretized on a triangular mesh shown in Fig. 2a. We use a control volume procedure essentially the same as that described in Prakash and Patankar [14], except that we have preferred to retain the central differencing scheme. In Prakash and Patankar [14] and related works, an exponential variation was introduced for stability at high cell Peclet numbers. Although such a differencing scheme provides stability, it reduces the accuracy to first order and is not satisfactory. The same is true of other first-order upwind schemes, which ensure stability, but lead to unacceptable large dissipative errors. It is possible to use higher-order upwind schemes that ensure both stability and accuracy, but we have retained central differencing for simplicity and second-order accuracy. Currently we have refined the finest mesh, until the cell Peclet number decreases below the stable value. Thus for a given grid, there exists a maximum flow Reynolds number that cannot be exceeded.

Figure 2a also shows the control volume constructed around a representative node P, by joining the centroids of the relevant triangles to the midpoints of the sides. The equations are integrated over each of these control volumes to obtain nodal values of pressure and velocity. The checker-board split in the pressure field that arises in such equal-order interpolation is avoided, by requiring a different set of velocities $(\tilde{u}, \tilde{v})$, located at the cell interfaces, to satisfy mass continuity. This practice is similar to the momentum interpolation concept used in collocated finite volume schemes for structured grids [15–17].

We now describe the details of the discretization procedure.

2.1. *The Discretization Scheme*

The Momentum Balances. Integrating Eq. (1) over the discrete control volume ABCDEF, we have

$$\int_V \nabla \cdot (\mathbf{u}u - \nu \nabla u)\, dV = \int_V \left(B_u - \frac{\partial p}{\partial x}\right) dV.$$

Using the divergence theorem, we can write the above equation as

$$\int_S [(\mathbf{u}u - \nu \nabla u) \cdot \mathbf{n}]\, dS = \int_V \left(B_u - \frac{\partial p}{\partial x}\right) dV, \tag{4}$$

where S is the enclosing surface of control volume V.

Consider now element PAB (Fig. 2(b)), which has two faces, a_1c and ca_3, bounding the control volume around P. The contributions from these two surfaces to the flux balance can be written as

$$\int_{a_1}^{c} (\mathbf{J}_u \cdot \mathbf{n})\, dS + \int_{c}^{a_3} (\mathbf{J}_u \cdot \mathbf{n})\, dS - \int_{Pa_1ca_3} \left(B_u - \frac{\partial p}{\partial x}\right) dV, \tag{5}$$

where

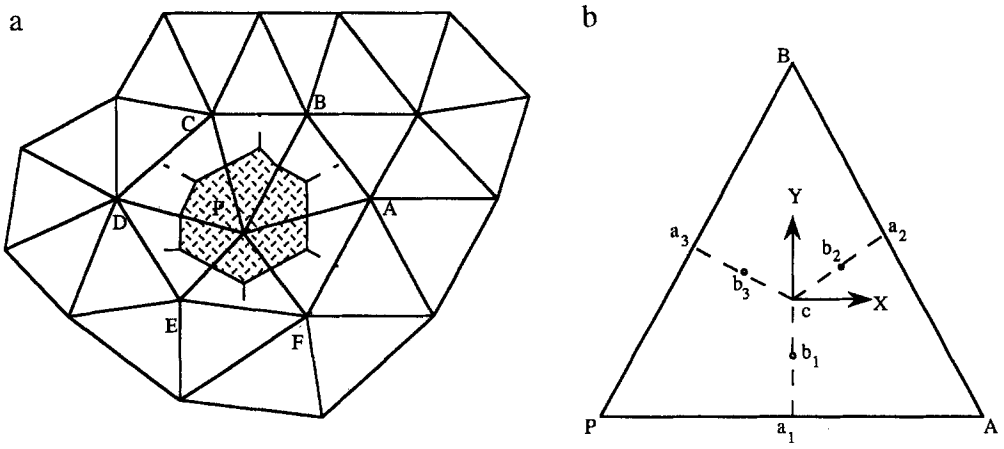

FIG. 2. (a) Unstructured mesh with control volume around node P. (b) Element PAB and local coordinate system.

$$\mathbf{J}_u = \mathbf{u}u - \nu\nabla u.$$

To compute the flux $\mathbf{J}_u$, we use a linear interpolation of velocities between the nodes of PAB. Thus,

$$\begin{aligned} u &= a_u x + b_u y + c_u \\ v &= a_v x + b_v y + c_v. \end{aligned} \tag{6}$$

The pressure p, likewise, assumed to vary linearly and is given by

$$p = a_p x + b_p y + c_p. \tag{7}$$

It is convenient to integrate the flux terms in local coordinates (X, Y), defined with the origin at the centroid of the element. This yields an expression for the contribution from element PAB to the equation at P as

$$\begin{aligned} &\frac{1}{\sqrt{X_{a_1}^2 + Y_{a_1}^2}} \int_{a_1}^{c} (X_{a_1} J_{uY} - Y_{a_1} J_{uX})\, dS + \frac{1}{\sqrt{X_{a_3}^2 + Y_{a_3}^2}} \\ &\times \int_{c}^{a_3} (Y_{a_3} J_{uX} - X_{a_3} J_{uY})\, dS - \left[B_u - \frac{\partial p}{\partial x}\right] \frac{A_{\mathrm{PAB}}}{3}, \end{aligned} \tag{8}$$

where $(\partial p/\partial x)$ is constant over the element PAB. Expanding J_{uX} and J_{uY}, the X and Y components of $\mathbf{J}_u$, using expressions for u, we get

$$\begin{aligned} J_{uX} &= (f_p u_p + f_A u_A + f_B u_B) u \\ &\quad - \nu \left(u_p \frac{\partial f_p}{\partial x} + u_A \frac{\partial f_A}{\partial x} + u_B \frac{\partial f_B}{\partial x} \right), \end{aligned} \tag{9}$$

where f_p, f_A, and f_B are linear shape functions. The integrals in Eq. (8) are evaluated by Simpson's rule, giving

$$\int_{a_1}^{c} J\, dS = |a_1 c|/6[J(a_1) + 4J(b_1) + J(c)]. \tag{10}$$

After collecting like terms and simplifying the complete equation, it can be shown that the resulting equation has the form

$$A_p u_p = \Sigma A_{nb} u_{nb} + V_p \left\langle B_u - \frac{\partial p}{\partial x} \right\rangle_p, \tag{11}$$

where u_p is the value of u at point P and u_{nb} represents values at the neighboring nodes A, B, C, D, E, and F. V_p is the area of the control volume around P, and $\langle\ \rangle$ is an average defined by

$$\langle B \rangle = (1/V_p) \sum_e [(A_i/3) B_i], \tag{12}$$

where A_i is the area of element i around P, and Σ_e denotes summation over all the elements contributing to V_p. The expressions for the coefficients are not provided here, but can be derived by the above-mentioned steps. Following the same procedure for Eq. (2), we can obtain the discretized y-momentum balance as

$$A_p v_p = \Sigma A_{nb} v_{nb} + V_p \left\langle B_v - \frac{\partial p}{\partial y} \right\rangle_p. \tag{13}$$

It is convenient to define momentum velocities $\hat{u}$ and $\hat{v}$ as

$$\hat{u} = (\Sigma A_{nb} u_{nb})/A_p, \quad \hat{v} = (\Sigma A_{nb} v_{nb})/A_p, \tag{14}$$

so that

$$u = \hat{u} + V_p \left\langle B_u - \frac{\partial p}{\partial x} \right\rangle / \mathrm{A}_p$$

and

$$v = \hat{v} + V_p \left\langle B_v - \frac{\partial p}{\partial y} \right\rangle / A_p. \tag{15}$$

The Continuity Equation. In the present procedure, u and v located at the nodal points do not satisfy the continuity equation. Rather, the cell face fluxes are balanced for each control volume. These cell face fluxes are interpolants of the nodal values in a special way that preserves the connections between the nodal pressures. The practice is similar to the momentum interpolation scheme used in finite volume schemes with a collocated arrangement of velocities and pressure [15–17].

We define a new set of velocities $\tilde{u}$ and $\tilde{v}$, located at the interfaces and related to $\hat{u}$ and $\hat{v}$ by

$$\begin{aligned} \tilde{u} &= \hat{u} + D\left(B_u - \frac{\partial p}{\partial x}\right) \\ \tilde{v} &= \hat{v} + D\left(B_v - \frac{\partial p}{\partial y}\right), \end{aligned} \tag{16}$$

where $D = V_p/A_p$. The pressure gradients in Eqs. (16) are evaluated locally for each element. The discrete continuity equation is obtained from

$$\nabla \cdot \tilde{\mathbf{u}} = 0, \tag{3}$$

written as

$$\int_S (\tilde{\mathbf{u}} \cdot \mathbf{n})\, dS = 0. \tag{17}$$

For each element enclosing the nodal control volume, there are two surfaces for which the above integral is to be evaluated. For element PAB,

$$\int_{a_1}^{c} (\tilde{\mathbf{u}} \cdot \mathbf{n})\, dS = \frac{1}{|a_1 c|} \int_{a_1}^{c} [X_{a_1}\tilde{v} - Y_{a_1}\tilde{u}]\, dS. \tag{18}$$

The integrals $\int_{a_1}^{c} \tilde{u}\, dS$ and $\int_{a_1}^{c} \tilde{v}\, dS$ are evaluated by Simpson's rule, together with the relations (16). The resulting contributions from interface a_1c is then

$$\begin{aligned} \int_{a_1}^{c} (\tilde{\mathbf{u}} \cdot \mathbf{n})\, dS = \frac{1}{6}\Bigg\{ & x_{a_1}\left[\hat{v}_{a_1} + 4\hat{v}_{b_1} + \hat{v}_c + \left(B_v - \frac{\partial p}{\partial y}\right)\right. \\ & \left. \times (D_{a_1} + 4D_{b_1} + D_c)\right] \\ & - Y_{a_1}\left[\hat{u}_{a_1} + 4\hat{u}_{b_1} + \hat{u}_c + \left(B_u - \frac{\partial p}{\partial x}\right)\right. \\ & \left. \times (D_{a_1} + 4D_{b_1} + D_c)\right]\Bigg\}. \end{aligned} \tag{19}$$

The values of D at points within the element are linearly interpolated from the nodal values. The pressure gradients $(\partial p/\partial x)$ and $(\partial p/\partial y)$ are now local at the cell faces and can be related to the nodal pressures (p_P, p_A, p_B) through the relations

$$\frac{\partial p}{\partial x} = \frac{\partial f_P}{\partial x} p_P + \frac{\partial f_A}{\partial x} p_A + \frac{\partial f_B}{\partial x} p_B$$

and

$$\frac{\partial p}{\partial y} = \frac{\partial f_P}{\partial y} p_P + \frac{\partial f_A}{\partial y} p_A + \frac{\partial f_B}{\partial y} p_B. \tag{20}$$

If the above equations are substituted in the two interface flux relations, the contributions from element PAB to the continuity at node P is obtained. Similar contributions from all elements surrounding P then provide a pressure equation at P given by

$$A_P^p p_P = \sum A_{nb}^p p_{nb} + M_p, \tag{21}$$

where M_P is the source term arising from the terms containing $\hat{u}$, $\hat{v}$ and B_u, B_v.

We now seek a solution (u, v, p) that satisfies the set of discrete equations (11), (13), and (21).

2.2. *Single Grid Solution Strategy*

The system of coupled equations (11), (13), and (21) is solved by a sequential solution method, SIMPLER [18]. The iterative update involves solving in a cycle the pressure equation, followed by the two momentum equations. Starting from guessed velocity and pressure fields, the coefficients A_P and A_{nb} are first assembled. Using these, the pressure equation is assembled through the above-mentioned formulae. The pressure equation is then solved by any convenient linear solver. For simplicity, we have used a point Gauss–Seidel scheme, which is repeated a few (nswpp) times. This pressure field is then used to solve the velocity equations. The previously assembled A_P and A_{nb} are used, and a few (nswpm) sweeps of the Gauss–Seidel scheme are made. The new velocity field is then used for calculating the next iterate of the pressure field.

In order to prevent the iterative process from becoming unstable, underrelaxation is used in the Gauss–Seidel scheme. This is done by adding only a part of the change to the flow variables. In an implicit manner, the discrete equations are modified as

$$A_P = A_P/\alpha, \quad A_P^p = A_P^p/\alpha,$$

and

$$B = B + (A_P/\alpha)(1 - \alpha)\phi_{\text{old}}, \tag{22}$$

where $B = V_P \langle B_u - (\partial p/\partial x)\rangle$, $V_P \langle B_v - (\partial p/\partial y)\rangle$, or M_P, and $\phi = u$, v, or p for the x- or y-momentum balance, or the pressure

equation, respectively. Due to the above modifications of the momentum equations, the velocities $\hat{u}$ and $\hat{v}$ are redefined to be

$$\hat{u} = (\sum A_{nb}u_{nb})/A_P + (1 - \alpha)u$$

and

$$\hat{v} = (\sum A_{nb}v_{nb})/A_P + (1 - \alpha)v, \tag{23}$$

where A_P now refers to the modified coefficient.

The above iterative procedure is convergent, but the rate of convergence deteriorates as the mesh is refined. As more and more nodes are employed to accurately resolve the flow features, the rate of convergence becomes prohibitively slow due to the low frequency errors. Therefore, a technique to accelerate the convergence is required. Here we have used the multigrid method that has been shown to work well for structured grids [5, 7, 19–24, 26].

2.3. *The Multigrid Method*

It is well known that a given mesh can efficiently smooth only those errors whose wavelengths are comparable to the mesh spacing. Therefore with very fine meshes, only a small portion of the error spectrum is efficiently removed. As the iterations progress, very soon the low frequency errors take over and degrade the convergence rate. The principle used in the multigrid method is that low frequency errors on a fine mesh transform to high frequency errors on coarser meshes. Hence, if the low frequency solution errors are transferred from a fine mesh to coarser meshes, relaxation on the coarse meshes can reduce these errors much faster than if only the fine mesh is used. Considerable acceleration can be achieved by using a sequence of coarse grids to which the errors are transferred (restricted) and smoothed, and subsequently interpolating (prolongating) the corrections to the finer grid.

Different cycling schemes are possible in any multigrid procedure. Here we have used a fixed V-cycle as the basic cycling strategy. In a fixed V-cycle, a prespecified number of iterations (relaxations) are performed on a given grid after which the residuals are restricted to the next coarser grid. After relaxation on the coarsest grid, the corrections to the solution are prolongated successively to the finer grids. Relaxations are performed also during the upward leg of the cycle. The fixed cycle is preferred here over an adaptive cycling strategy since it is not always possible to assign an optimal smoothing rate as is required in an adaptive strategy. The coarse grids can also be used to generate good initial solutions for adjacent finer grids. The multigrid scheme can be arranged as a nested iteration sequence in which the solution to the flow field is initiated on the coarsest grid and better and better estimates of the flow are obtained by successive prolongation and relaxation of the converged solutions. This is frequently referred to as the full multigrid procedure (FMG).

Details of the Present Implementation. Mesh generation and refinement. In the present procedure, the coarsest mesh is first generated as for any single grid procedure, by the Delaunay triangulation method. Subsequent finer grids are then generated by successively dividing each element into four elements (Fig. 3a). A prespecified number of nested grids are thereby obtained. Each coarse grid element shares three nodes with the daughter finer grid elements. This grid arrangement makes the intergrid transfers as well as the construction of coarse grid equations simple.

The coarse grid discrete equations. Successful multigrid procedures rely heavily on consistent practices for the construction of the coarse grid equations and for the restriction and prolongation operators. Consistent restriction of variables and residuals to the coarser grids is the most important aspect of multigrid procedures for a system of equations, especially the fluid flow equations. For nonlinear equations, the full approximation scheme (FAS) is the most suitable scheme for deriving the coarse grid equations. This is an extension of the more straightforward correction scheme (CS) that is used for linear equations.

Consider the discrete fine grid equations given by

$$\mathbf{L}^f\mathbf{q}^f = \mathbf{F}^f, \tag{24}$$

where $\mathbf{L}^f$ is the nonlinear operator matrix made of the convection and diffusion terms, $\mathbf{q}^f$ is the solution vector, and $\mathbf{F}^f$ is the right-hand side vector. The superscript f is used to denote the fine grid. After a few iterations on the fine grid, the residual is computed as

$$\mathbf{R}^f = \mathbf{F}^f - \mathbf{L}^f\mathbf{q}^f. \tag{25}$$

This residual is restricted to the next coarser grid, and it is required that the corrections satisfy the equation

$$\mathbf{L}^{f-1}\,\Delta\mathbf{q}^{f-1} = I_f^{f-1}\mathbf{R}^f, \tag{26}$$

where $\mathbf{L}^{f-1}$ is the nonlinear operator on the coarse grid, $\Delta\mathbf{q}^{f-1}$ is the vector of corrections on the coarse grid, and I_f^{f-1} is the restriction operator. For the FAS scheme, Eq. (26) is rewritten as

$$\begin{aligned}\mathbf{L}^{f-1}(\Delta\mathbf{q}^{f-1} + I_f^{f-1}\mathbf{q}^f) &= I_f^{f-1}\mathbf{R}^f + \mathbf{L}^{f-1}(I_f^{f-1}\mathbf{q}^f)\\ &= \mathbf{F}^{f-1} + I_f^{f-1}\mathbf{R}^f - (\mathbf{F}^{f-1} - \mathbf{L}^{f-1}(I_f^{f-1}\mathbf{q}^f)).\end{aligned} \tag{27}$$

This can be written as

$$\mathbf{L}^{f-1}\mathbf{q}^{f-1} = \mathbf{F}^{f-1} + (I_f^{f-1}\mathbf{R}^f - \mathbf{R}_0^{f-1}), \tag{28}$$

where $\mathbf{R}_0^{f-1}$ is the residual on the coarse grid, calculated using the restricted solution vector, and $\mathbf{q}^{f-1}$ is the solution on the coarse grid. After a fixed number of iterations on the coarse

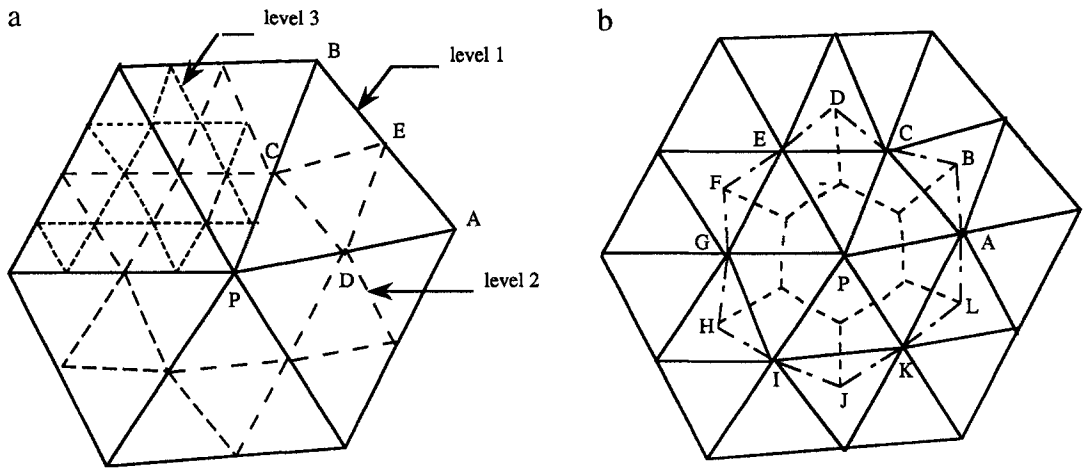

FIG. 3. (a) Mesh refinement. (b) Coarse and fine grid control volumes around node P.

grid, the corrections implied by the coarse grid solution can be extracted from the relation

$$\Delta \mathbf{q}^{f-1} = \mathbf{q}^{f-1} - I_f^{f-1}\mathbf{q}^f. \tag{29}$$

The above FAS scheme is used in a straightforward way for the momentum equations. The restriction and prolongation operators defined below provide a consistent and convergent multigrid procedure. The main complexity in the present scheme lies in the construction of the pressure equation which satisfies mass continuity, not for the nodal velocities, but for a different set of fluxes implicitly located at the cell faces of the control volume. As the success of the present procedure relies solely on this aspect, we give below details of the coarse grid pressure equation.

The FAS form of the coarse grid pressure equation that results from the continuity satisfaction condition is derived as follows. We begin with the correction equation

$$(\nabla \cdot \tilde{\mathbf{u}}')^{f-1} = I_f^{f-1} R_c^f, \tag{30}$$

where the prime denotes the correction in $\tilde{\mathbf{u}}$, and the right-hand side is the restricted residual in the continuity equation. Equation (30) is expressed as

$$\nabla \cdot (\tilde{\mathbf{u}} + \tilde{\mathbf{u}}')^{f-1} = I_f^{f-1} R_c^f + (\nabla \cdot \tilde{\mathbf{u}})^{f-1}. \tag{31}$$

Now,

$$\tilde{u} = \hat{u} + D\,\tilde{\nabla} p$$

and

$$\tilde{v} = \hat{v} + D\,\tilde{\nabla} p, \tag{32}$$

where $\hat{\mathbf{u}}$ is the momentum velocity and $\tilde{\nabla} p$ is the pressure gradient that is used to evaluate the cell face fluxes. For the coarse grid equations, the components of $\hat{\mathbf{u}}$ are defined as

$$\hat{u} = (R_u + \Sigma A_{nb} u_{nb})/A_P + (1 - \alpha)u$$

and

$$\hat{v} = (R_v + \Sigma A_{nb} v_{nb})/A_P + (1 - \alpha)v, \tag{33}$$

where R_u and R_v are the net coarse grid momentum residuals defined from Eq. (28) as

$$R = I_f^{f-1} R^f - R_0^{f-1}. \tag{34}$$

Substituting Eqs. (32) in (31), the coarse grid continuity equation is given by

$$\nabla \cdot (\hat{u} + D\,\tilde{\nabla} p + \hat{u}' + D\,\tilde{\nabla} p')^{f-1} = I_f^{f-1} R_c^f + \nabla \cdot (\hat{u} + D\,\tilde{\nabla} p)^{f-1}, \tag{35}$$

where p^{f-1} is the restricted pressure $I_f^{f-1} p^f$. Equation (35) can be further rewritten as

$$\begin{aligned} \nabla \cdot (D\,\tilde{\nabla} p + D\,\tilde{\nabla} p')^{f-1} &= I_f^{f-1} R_c^f - \nabla \cdot \hat{u}^{f-1} \\ &\quad + (\nabla \cdot D\,\tilde{\nabla} p + \nabla \cdot \hat{u})^{f-1} \\ &= I_f^{f-1} R_c^f - \nabla \cdot \hat{u}^{f-1} + R_{c0}^{f-1} \end{aligned} \tag{36}$$

where R_{c0}^{f-1} is the coarse grid residual in the pressure equation calculated using the restricted values of the variables. It must be noted that because of the segregated method of solution, $\hat{u}'$ is set to zero for the pressure equation. Now, in the FAS practice, the left-hand side terms of Eq. (36) can be combined to give

$$\nabla \cdot (D\,\tilde{\nabla} p)^{f-1} = -\nabla \cdot \hat{u}^{f-1} + R_c^{f-1}, \tag{37}$$

where p^{f-1} is now redefined to be

$$p^{f-1} = I_f^{f-1} p^f + (p')^{f-1} \tag{38}$$

and

$$R_c^{f-1} = I_f^{f-1} R_c^f + R_{c0}^{f-1}. \tag{39}$$

Equation (37) has the standard structure of the pressure equation with an added residual R_c^{f-1}.

Restriction and prolongation operations. Restriction and prolongation operators for structured rectangular and curvilinear grids are now well established [7, 15, 21]. For an arbitrarily generated sequence of unstructured grids the integrid transfers must be performed through systematic interpolations using appropriate geometric coordinates of the variable locations [25]. An advantage of constructing fine grids embedded within the coarse grids is that the simple injection scheme can be used as the restriction operator for the nodal variables. Thus coarse grid values for (u, v, p) are obtained by locating the fine grid daughter nodes coincident with the considered coarse grid nodes.

For the residuals in the momentum equations, several fine grid residuals are summed to obtain the corresponding coarse grid residual $I_f^{f-1}\mathbf{R}^f$. We need to determine the fractions of the fine grid control volumes around a coarse grid node that contribute to the coarse grid control volume (see Fig. 3b). The coarse grid control volume around P in two dimensions is given by the area ABCDEFGHIJKL. This is composed of fractions of the fine grid control volumes around each of the nodes P, A, B, ... and L. It is apparent that the complete fine grid control volume around P contributes to the coarse grid volume. It can be shown that the rest of the coarse grid volume is made of the sum of half the fine grid volumes around each of the nodes A, B, ... and K. Therefore, the restricted residual at point P is the sum of the fine grid residual at point P and half the fine grid residuals at the surrounding fine grid nodes.

The prolongation process similarly is considerably simplified because of the mesh embedding. Coarse grid corrections to the solution are prolongated by direct injection at those fine grid nodes that coincide with the coarse nodes. For those fine grid nodes that lie in between the coarse nodes, the corrections are determined as averages of the corrections at the two surrounding coarse nodes. For example, in Fig. 3a, the coarse grid corrections at nodes P, A, and B are injected onto the next finer grid, whereas the corrections at a node such as D are determined as averages of the corrections at P and A.

3. RESULTS AND DISCUSSION

Flow in the triangular cavity was simulated for Reynolds numbers of 50, 100, 400, and 800, where the Reynolds number is defined with respect to the top wall velocity and the depth of the cavity. Since the magnitude of the top wall velocity was taken to be 1, Reynolds number Re = $4/\nu$. For each value of Re used, because of the absence of upwinding, a certain level of refinement of the mesh was required for convergence of the scheme. A total of six grid levels was used for all the computations. The coarsest mesh used had 35 nodes and 48 elements, and the finest had 24897 nodes and 49152 elements. As mentioned in the previous section, multigrid cycling between the grids was used to accelerate the convergence of the scheme. In general, CPU time increased with Reynolds number for the same mesh, in proportion to the number of iterations for convergence, and varied linearly with number of mesh points as a result of multigrid efficiency. Figure 4 shows for Re = 400 the dramatic improvement in the convergence rate with the multigrid method, as compared with the single grid scheme. In addition, Richardson extrapolation was used to get the solution for a still higher refinement. The extrapolation was done as follows. Let f represent the discrete solution to a given equation on a mesh of spacing h. It is assumed that f has a series representation of the form

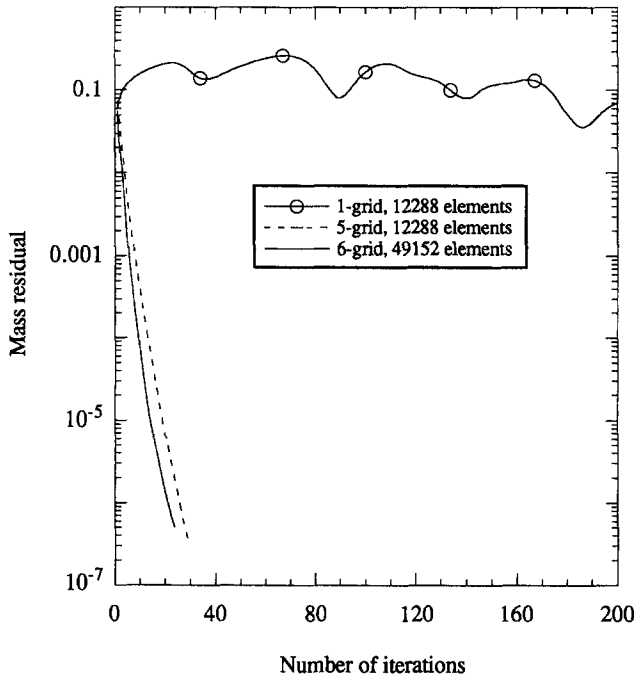

FIG. 4. Multigrid and single grid convergence for Re = 400.

$$f = f(\text{exact}) + g_1 h + g_2 h^2 + g_3 h^3 + \cdots. \tag{40}$$

It is sufficient that Eq. (40) be a valid definition for the order of the discretization. Here g_1, g_2, etc. are functions that do not depend on the discretization. For a second-order method such as the one used here, $g_1 = 0$. For the extrapolation, two discrete solutions, f_1 and f_2, obtained on distinct grids of spacing h_1 and

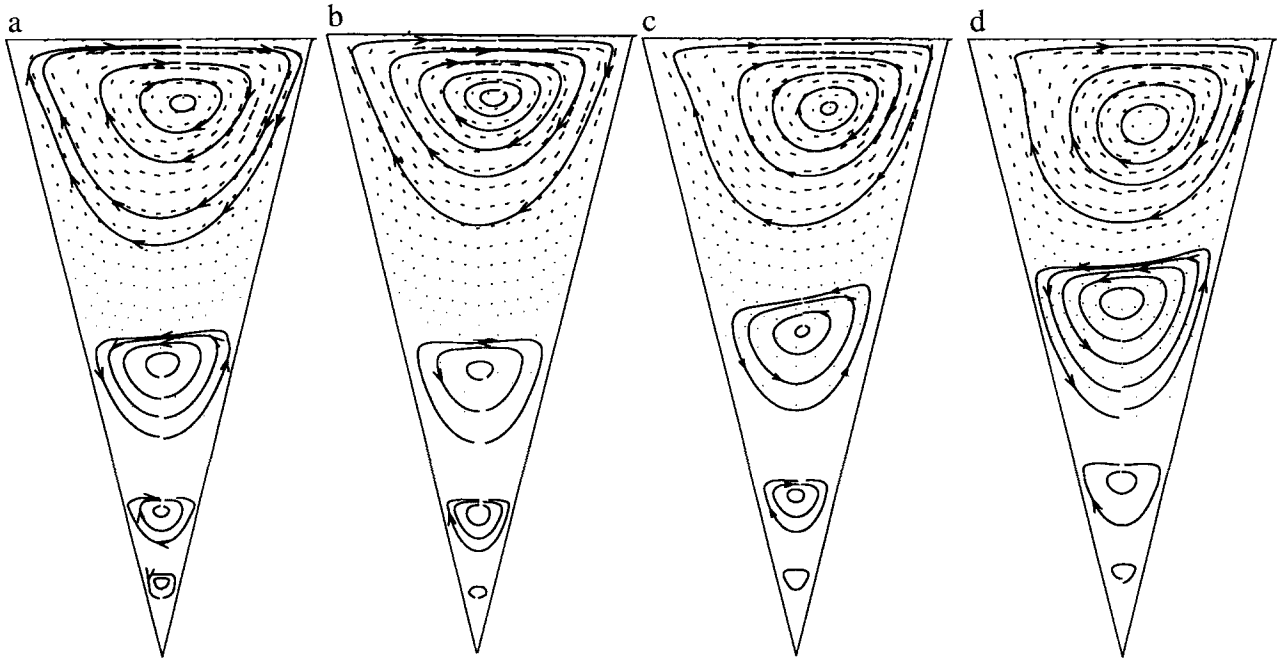

FIG. 5. Streamtraces and velocity vectors for (a) Re = 50, (b) Re = 100, (c) Re = 400, and (d) Re = 800.

h_2, respectively, are used to eliminate g_2 from Eq. (40). As a result, we obtain

$$f(\text{exact}) = (h_2^2 f_1 - h_1^2 f_2)/(h_2^2 - h_1^2) + \text{higher order terms.} \quad (41)$$

If we neglect the higher order terms in Eq. (41), we get a new solution that is at least third-order accurate and given by

$$f(\text{exact}) \approx f_1 + (f_1 - f_2)/(r^2 - 1), \quad (42)$$

where $r = h_2/h_1$. For the sequence of grids that we have used, $r = 2$. If h_1 and h_2 are small enough, then Eq. (42) represents a more accurate solution than f_1 and f_2.

The procedure was found to be fairly sensitive to the value of α, the underrelaxation factor in the Gauss–Seidel scheme. In the present study, α was varied from 0.5 to 0.9. For Re $\leq$ 400, $\alpha = 0.7$ was found to be optimum, while for Re = 500 and 800, it had to be decreased to 0.6 and 0.5, respectively.

Figures 5a–d show the streamtraces in the flowfield for Re = 50, 100, 400, and 800, respectively. These are plots of the particle trajectories in the flow field. There is a slight mismatch in the starting and ending points of some of these trajectories, especially in Fig. 5d, because of the small errors in the solution (O (10^{-6})) of nearly the same order as the velocity in this region. Let us now examine the features of the flowfield shown. All figures show similar eddies of decreasing size towards the lower corner of the cavity. For all Reynolds numbers, the lower three eddies have their centers along the centerline of the cavity. The topmost eddy, where inertial effects are dominant, first moves to the right as Re increases and later moves back towards the center of the cavity, while the lower eddies remain unaffected. This is in keeping with Moffat's [12] observation that close to the stationary corner, the flowfield is independent of any disturbance far away from it. Further, as determined by Moffat, the distances of the lower three edies from the corner follow a geometric sequence. This is observed for all values of Re reported here. In particular, for Re = 50, all eddy centers show the sequence, i.e., $(Y_2/Y_1) \approx (Y_3/Y_2) \approx (Y_4/Y_3) \approx 2$, where Y_i is the distance of the ith eddy from the lower corner. The topmost eddy deviates from this sequence with increase in Reynolds number, since inertial effects near the top wall become more important as Re increases. It must be noted that Moffat's analysis is valid only in those regions where inertial effects are negligible. Therefore, for Re = 800, $(Y_2/Y_1) \approx (Y_3/Y_2) \approx 2$, while $(Y_4/Y_3) \approx 1.5$. A similar sequence for the eddy intensities is observed, as will be seen shortly.

Figures 6a and b show plots of the x-velocity along the centerline of the cavity for Re = 50 and 800, respectively. If the ordinate of these plots is enlarged, detailed information about the eddies is obtained. For those eddies which lie symmetrically about the centerline, u along the centerline vanished at their centers. Therefore, the points where the curve intersects the x-axis coincide with the centers of all eddies except the topmost. Further, the maxima in these plots give a measure of the intensities of the respective eddies (see [12]). If I_i is the intensity of the ith eddy from the lower corner, then for Re = 50, $(I_2/I_1) \approx (I_3/I_2) \approx (I_4/I_3) \approx 400$, while for Re = 800, $(I_2/I_1) \approx (I_3/I_2) \approx 400$, and $(I_4/I_3) \approx 30$. Here again it is seen

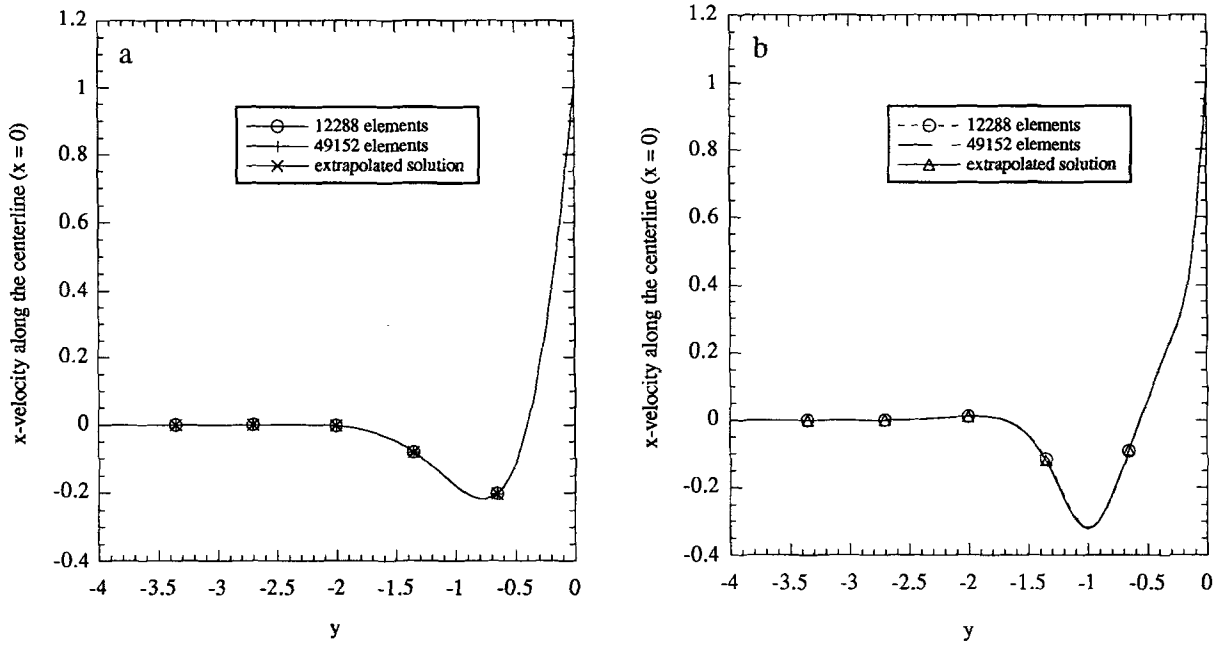

FIG. 6. Centerline x-velocity variation for (a) Re = 50 and (b) Re = 800.

that the intensities of the eddies for low Reynolds numbers follow a geometric sequence. It was shown by Moffat [12] that both ratios (Y_{i+1}/Y_i) and (I_{i+1}/I_i) are functions of only the stationary corner angle. As this angle increases, both ratios increase rapidly, till no eddies are observed for angles greater than 146°. In particular, up to angle of 40°, adjacent eddies are of comparable size, but for larger corner angles, the ratio (Y_{i+1}/Y_i) increases rapidly to about 10 for an angle of 90°. This is probably the reason why for the equilateral triangle studied by Ribbens *et al.* [11], only the topmost eddy could be resolved. The lower eddies were probably too small to be captured on the grids used by them. This is also the reason why we chose

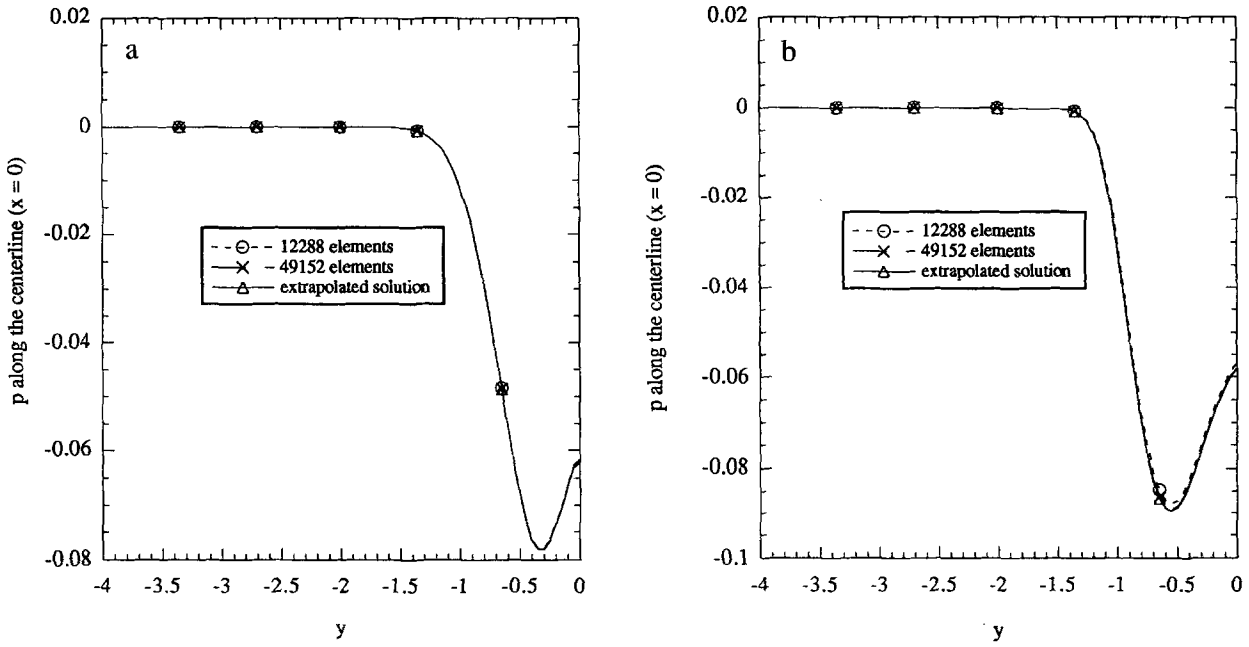

FIG. 7. Centerline pressure variation for (a) Re = 50 and (b) Re = 800.

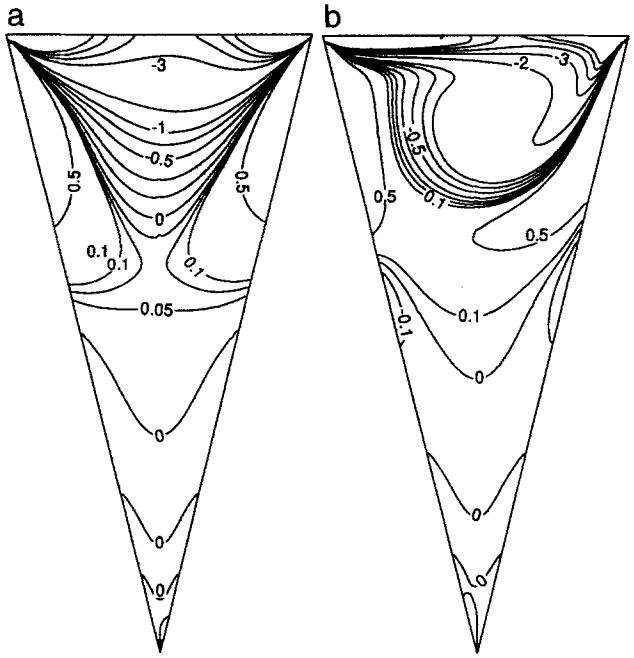

FIG. 8. Contours of constant vorticity for (a) Re = 50 and (b) Re = 800.

a smaller corner angle in our study, so that we could observe more than one eddy in the flow field.

Figures 7a and b show the plots of pressure along the centerline for Re = 50 and 800, respectively. It is seen that variations in pressure are observed only close to the top wall. The pressure field then quickly levels off to a constant value in the lower region.

Plots of the contours of constant vorticity defined as $\omega = [(\partial v/\partial x) - (\partial u/\partial y)]$ are shown in Figs. 8a and b for Re = 50 and 800, respectively. It is seen that for small Re, the vorticity field is symmetrical about the centerline. However, as Re increases, the vorticity variation moves to the boundary regions of the cavity, while the interior of the topmost eddy tends to attain constant vorticity. The simulations could not be carried out for high enough Reynolds numbers to verify Batchelor's [13] analytical predictions for inviscid flow. However, from the trend of the vorticity plots, it can be conjectured that for high enough Reynolds numbers, there will be only a thin boundary layer of vorticity variation around the topmost eddy, with an inner region of constant vorticity. Figures 9a and b show the plots of vorticity along the centerline for Re = 50 and 800, respectively. Here it appears that on the scale of the graph, most of the vorticity variation is near the top wall, where there is maximum shear.

Figures 6, 7, and 9 also show plots of the solution at two different mesh sizes and of an extrapolated solution. These indicate the accuracy of the solution obtained. In order to report grid-independent results, the simple but effective technique of Richardson extrapolation is often employed [26–28]. Here, as mentioned earlier, the solution on two consecutive grids is used to extrapolate to a solution of higher accuracy. If the two grids are sufficiently fine, good convergence is observed to the extrapolated solution. This is indeed seen for the grids used here (Figs. 6, 7, and 9). The curves of Figs. 7a and b have been obtained by subtracting a constant reference pressure from the

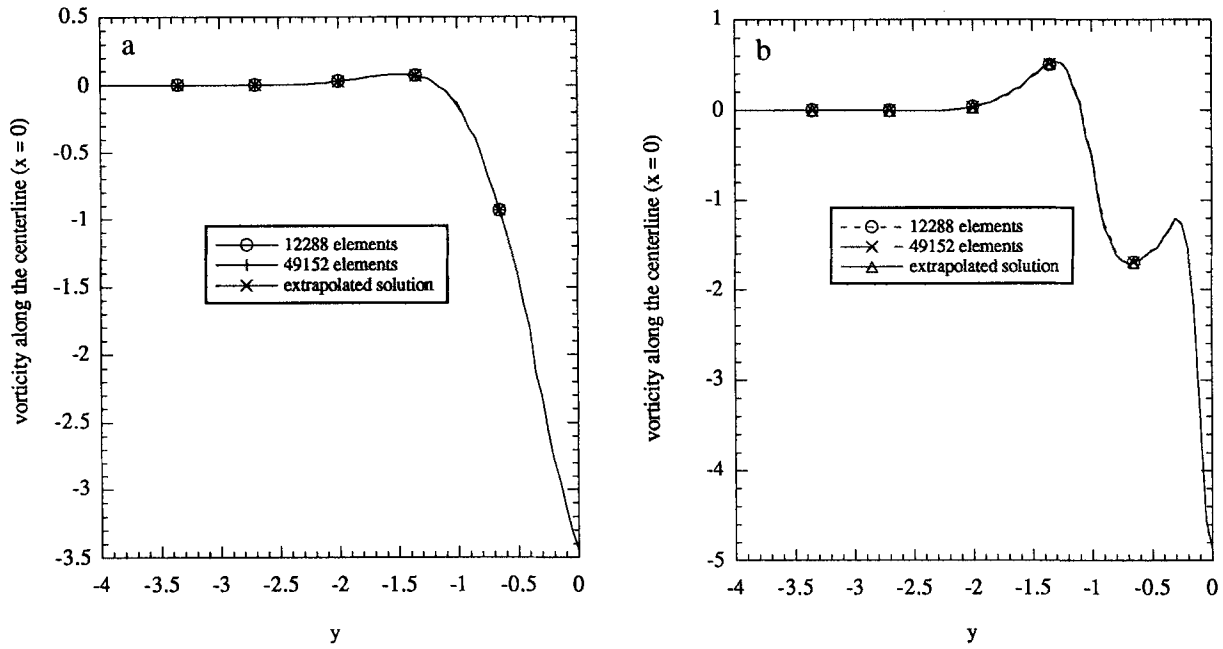

FIG. 9. Centerline vorticity variation for (a) Re = 50 and (b) Re = 800.

TABLE I

Characteristics of the Flow Field for Different Reynolds Numbers

Reynolds number	Location of the eddy centers				Extrema in the centerline x-velocity
50	(0, −3.550)	(0, −3.092)	(0.002, −2.182)	(0.050, −0.395)	5.8×10^{-4} −0.219
100	(0, −3.545)	(0, −3.085)	(0.005, −2.162)	(0.097, −0.400)	6.4×10^{-4} −0.218
400	(0, −3.475)	(0, −2.950)	(0.040, −1.882)	(0.225, −0.450)	2.7×10^{-3} −0.242
800	(0, −3.427)	(0, −2.852)	(0.000, −1.695)	(0.153, −0.545)	0.0116 −0.323

pressure field. This does not alter the solution, because in incompressible flows, only the gradients of pressure appear in the equations.

Table I summarizes the important characteristics of the flow at the four Reynolds numbers reported. The extrapolated values are not reported separately, since in the graphical method used to determine the values, there were imperceptible differences between the numerical solution and the extrapolated one. Table I may be used for benchmarking other numerical solutions.

4. SUMMARY AND CONCLUSIONS

In this paper, we have presented the results of a steady viscous flow simulation in a triangular cavity. With the use of triangular grids and a multigrid method, the solution was obtained without encountering any of the difficulties reported for structured grid-based methods [11]. The most significant flow feature was the occurrence of a sequence of eddies of rapidly decreasing size and intensity towards the lower stationary corner of the cavity. The attributes of these eddies and of the vorticity distribution were successfully verified with the analytical predictions of Moffat [12]. Richardson extrapolation was used to ascertain grid independence of the results. Extensions of this work are currently being pursued. They include the use of adaptive refinement in place of uniform refinement to obtain the solution for higher Reynolds numbers, and the use of the present numerical procedure for simulating flows in more complex geometries with Neumann and periodic boundary conditions and with unsteady terms.

REFERENCES

1. O. R. Burggraf, *J. Fluid Mech.* **24,** 113 (1966).
2. F. Pan and A. Acrivos, *J. Fluid Mech.* **28,** 643 (1967).
3. J. D. Bozeman and C. Dalton, *J. Comput. Phys.* **12,** 348 (1973).
4. M. Nallasamy and K. Krishna Prasad, *J. Fluid Mech.* **79,** 391 (1977).
5. U. Ghia, K. N. Ghia, and C. T. Shin, *J. Comput. Phys.* **48,** 387 (1982).
6. R. Schreiber and H. B. Keller, *J. Comput. Phys.* **49,** 310 (1983).
7. S. P. Vanka, *J. Comput. Phys.* **65,** 138 (1986).
8. M. Vynnycky and S. Kimura, *Phys. Fluids A* **6,** 3610 (1994).
9. C. J. Ribbens, C.-Y. Wang, L. T. Watson, and K. A. Alexander, *Comput. Fluids* **20,** 111 (1991).
10. J. H. Darr and S. P. Vanka, *Phys. Fluids A* **3,** 385 (1991).
11. C. J. Ribbens, L. T. Watson, and C.-Y. Wang, *J. Comput. Phys.* **112,** 173 (1994).
12. H. K. Moffat, *J. Fluid Mech.* **18,** 1 (1963).
13. G. K. Batchelor, *J. Fluid Mech.* **1,** 177 (1956).
14. C. Prakash and S. V. Patankar, *Numer. Heat Transfer* **8,** 259 (1985).
15. K. M. Smith, W. K. Cope, and S. P. Vanka, *Int. J. Numer. Methods Fluids* **17,** 887 (1993).
16. C. M. Rhie and W. L. Chow, *AIAA J.* **21,** 1525 (1983).
17. M. Peric, R. Kessler, and G. Scheurer, *Comput. Fluids* **16,** 389 (1988).
18. S. V. Patankar, *Numerical Heat Transfer* (Hemisphere, Washington, DC, 1980).
19. R. E. Phillips and F. W. Schmidt, *Numer. Heat Transfer* **8,** 573 (1985).
20. W. Schroder and D. Hanel, *Comput. Fluids* **15,** 313 (1987).
21. M. C. Thompson and J. H. Ferziger, *J. Comput. Phys.* **82,** 94 (1989).
22. L. Fuchs and H. S. Zhao, *Int. J. Numer. Methods Fluids* **4,** 539 (1984).
23. D. S. Joshi and S. P. Vanka, *Numer. Heat Transfer B* **20,** 61 (1990).
24. P. M. Sockol, *Int. J. Numer. Methods Fluids* **8,** 417 (1993).
25. R. Löhner and K. Morgan, *Int. J. Numer. Methods Eng.* **24,** 101 (1987).
26. G. De Vahl Davis, *Int. J. Numer. Methods Fluids* **3,** 249 (1983).
27. M. Hortmann, M. Peric, and G. Scheuerer, *Int. J. Numer. Methods Fluids* **11,** 189 (1990).
28. P. J. Roache, *J. Fluids Eng.* **116,** 405 (1994).